

CrossMark
click for updatesHPSTAR
083_2015

Cite this: DOI: 10.1039/c5dt00426h

Impact of hydrostatic pressure on the crystal structure and photoluminescence properties of Mn⁴⁺-doped BaTiF₆ red phosphor†

Yonggang Wang,^{*a,b,c} Ting Wen,^c Lingyun Tang,^b Liuxiang Yang,^b Wenge Yang^{*b,d} and Yusheng Zhao^{*a}

High-efficiency red phosphors with non-rare-earth activators are emerging as an alternative for next generation solid-state warm white LEDs. Their optical properties depend strongly on the local site symmetry and the crystal field strength. Herein we present the pressure tuning of structural and photoluminescence (PL) properties of Mn⁴⁺-doped BaTiF₆ up to 40 GPa. *In situ* high pressure synchrotron X-ray diffraction, Raman and PL spectroscopy studies show that the crystal symmetry changes from trigonal at ambient pressure to monoclinic from 0.5 GPa and triclinic above 14 GPa, attributed to the distortion of (Ti/Mn)F₆ octahedra. The red emission peaks shift monotonically to longer wavelengths due to the reinforced crystal field strength within MnF₆ octahedra as pressure increases. A detailed comparison of emission shift rate, PL intensity and FWHM between Mn⁴⁺-doped BaTiF₆ and ruby (Cr³⁺-doped Al₂O₃) was performed using neon pressure transmission medium. This demonstration provides not only an efficient way to artificially tune the emission properties of practically useful phosphors by means of hydrostatic pressure, but also alternative candidates as potential pressure gauges for high pressure techniques.

Received 29th January 2015,

Accepted 14th March 2015

DOI: 10.1039/c5dt00426h

www.rsc.org/dalton

Introduction

Since the discovery of high-power blue InGaN/AlGaN LEDs by Nakamura *et al.* in 1994,¹ solid-state white light-emitting diodes (WLEDs) based on the combination of blue chips and yellow-emitting phosphors (*e.g.*, YAG:Ce³⁺) have attracted great scientific and industrial attention for their high energy efficiency, long lifetime and eco-friendship.^{2–5} However, warm WLEDs for indoor lighting purpose are difficult to be realized only with such yellow phosphors because of the lack of red light component. It is necessary to exploit novel red-emitting phosphors and integrate them into the packages of WLEDs to reach a high color-rendering index (CRI) and low correlated color temperature (CCT).^{6–10} Currently, a rare-earth activator is the most promising approach for energy efficient red phos-

phors for fluorescent lamps and WLEDs. The most successful materials are rare-earth-doped sulfates and (oxy)nitrides,^{11–18} such as Eu²⁺-doped CaS, Eu³⁺-doped Y₂O₂S and Eu²⁺-doped CaAlSiN₃. Nevertheless, the poor chemical stability and critical syntheses conditions of these air- and moisture-sensitive sulfides/nitrides make them unfavorable as competitive candidates for advanced WLEDs.

Mn⁴⁺-doped fluorides, with cheap host materials and non-rare-earth elements as activators, are emerging as an alternative for next generation solid-state warm WLEDs.^{19–22} Up to now, a series of Mn⁴⁺-activated alkaline or alkaline-earth metal fluorides have been reported exhibiting a strong absorption band that matches well with InGaN/AlGaN LEDs in the blue region and red emissions with high efficiency.^{23–33} The host materials include K₂SiF₆, Na₂SiF₆, K₂TiF₆, K₂ZrF₆, Na₂ZrF₆, BaSiF₆, BaTiF₆, *etc.* Most of these compounds with Mn⁴⁺-doping can be easily prepared under hydrothermal conditions or by low-temperature co-precipitation approaches,^{29–31} without special isolation from air or moisture. Very recently, a facile and efficient cation-exchange route has been proposed by Chen's group³⁴ to synthesise Mn⁴⁺-doped K₂TiF₆ with photoluminescence (PL) quantum yield as high as 98%. High-performance WLEDs with high CRI ($R_a = 81$), low CCT (3556 K) and luminous efficacy as high as 116 lm W⁻¹ have been fabricated based on this phosphor. These explorations show great promise of Mn⁴⁺-activated fluorides as cheap red phosphors for commercial warm WLEDs.

^aHigh Pressure Science and Engineering Center, University of Nevada, Las Vegas, Nevada 89154, USA. E-mail: ygygwang@gmail.com, yusheng.zhao@unlv.edu

^bHigh Pressure Synergetic Consortium (HPSynC), Geophysical Laboratory, Carnegie Institution of Washington, Argonne, IL 60439, USA. E-mail: wyang@ciw.edu

^cInstitute of Nanostructured Functional Materials, Huanghe Science and Technology College, Zhengzhou, Henan 450006, China

^dCenter for High Pressure Science and Technology Advanced Research (HPSTAR), Pudong, Shanghai 201203, China

†Electronic supplementary information (ESI) available: SEM image of Mn⁴⁺-doped BaTiF₆; Raman vibration modes of octahedrally coordinated TiF₆; emission spectra of ruby (Cr³⁺-doped Al₂O₃). See DOI: 10.1039/c5dt00426h

Since Mn^{4+} is a transition metal ion with $3d^3$ electron configuration, the optical properties of Mn^{4+} -activated materials can be strongly influenced by the doping site symmetry and the Mn-ligand hybridization according to the crystal field theory. A frequently used strategy to control the emission properties of phosphors is the chemical substitution method, by which chemical pressure can be generated by the neighboring-cation size-mismatch effect. For example, in Eu^{2+} -doped $\text{MSi}_2\text{O}_2\text{N}_2$ ($M = \text{Ca}, \text{Sr}, \text{Ba}$), both oxide/nitride and various cation substitutions are used to shift the emission spectra systematically and optimize the PL properties.^{35,36} A local anion clustering mechanism is proposed for such a cation mismatch effect and also predicted to be general to other oxynitride materials. In another phosphor Eu^{2+} -doped CaAlSiN_3 ,³⁷ cation-doping with different valences ($\text{La}^{3+}/\text{Li}^+$ to replace Ca^{2+}) can lead to a remote control effect that guides Eu^{2+} activators into selective Ca^{2+} sites, and thus can tune the optical properties efficiently. While, in Ce^{3+} -doped $\text{Sr}_{1-x}\text{Y}_{1+x}\text{Si}_4\text{N}_{6-x}\text{C}_x$,³⁸ the covalency of Ce^{3+} -N bonding is found to be reduced by high-valence doping, and the system can emit blue, green and yellow lights as x increases from 0 to 1. In all of the above-mentioned examples, systematic tuning of thermal quenching behavior is also observed.

Besides chemical doping, another powerful tool to tune the crystal field strength is applying pressure. Pressure as one of the state parameters can vary the crystal and electronic structures effectively by reducing the inter-atomic distances.³⁹ Many efforts toward the structure and property modulations and discovery of hidden phenomena have been achieved by various high pressure techniques.⁴⁰ As for the PL spectroscopy of transition metal activators within specific host lattices, it is often adopted for the following purposes in the high pressure applications: (1) to generate optimized or novel optical properties;^{41,42} (2) to be used as a structure probe;^{43–45} (3) to be used as a pressure standard.^{46,47} In this work, we investigate the pressure effect on the structure and photoluminescence properties of a Mn^{4+} ion in BaTiF_6 host material. The first aim is to study the impact of hydrostatic pressure on the red emission of Mn^{4+} -doped BaTiF_6 as an alternative crystal-field tuning method other than chemical doping. The other aim is to exploit Mn^{4+} spectroscopy within specific host lattices as a useful pressure gauge for the diamond anvil cell (DAC) techniques. As mentioned above, the application of high pressure allows us to realize a continuous crystal-field tuning of Mn^{4+} in the octahedrally coordinated sites. The material shows two pressure-induced phase transitions associated with crystal symmetry changes and linear red-shifts of the emission peak up to about 40 GPa. These results demonstrate hydrostatic pressure as an efficient tool to tune the emission properties of transition metal activated phosphors for practical usage. Detailed comparisons of the emission behavior under hydrostatic pressure between Mn^{4+} -doped BaTiF_6 and ruby (Cr^{3+} -doped Al_2O_3) were also performed. Due to their stable emission properties under high pressure, low-cost and facile synthesis route, Mn^{4+} -doped BaTiF_6 and other Mn^{4+} -doped fluorides may find applications in high pressure techniques.

Experimental

Material syntheses

Mn^{4+} -doped BaTiF_6 microcrystals were prepared *via* a facile one-step hydrothermal method. In a typical synthesis procedure, the starting materials 0.8765 g BaF_2 (5.0 mmol, A.R.), 0.3994 g TiO_2 (5.0 mmol, A.R.), 0.031 g KMnO_4 (0.2 mmol, A.R.), 10 ml HF (40% wt) and 30 ml distilled water were mixed thoroughly in a Teflon beaker by vigorous stirring for 30 minutes. Then the suspension was transferred to a 50 ml Teflon vessel and sealed in a stainless steel autoclave. After heating at 120 °C for 5 hours, the autoclave was allowed to cool down to room temperature by power off. Then the resulting white powders were filtered, washed with distilled water and alcohol several times, and finally dried at 80 °C under vacuum for 5 hours. The product yield was calculated to be 93% based on TiO_2 .

Characterization

Powder X-ray diffraction (XRD) data at ambient pressure were collected at room temperature (25 °C) on a Bruker D8 Advance diffractometer using germanium monochromatic $\text{Cu K}\alpha$ (40 kV and 40 mA). The data were collected in the 2θ range of 8–120° at a step size of 0.02° with an acquisition time of 1 s per step. Scanning electron microscopy (SEM) images and energy dispersive X-ray spectroscopy (EDS) were performed using FEI Quanta-250 with an accelerating voltage of 20 kV. The ambient photoluminescence excitation (PLE) and PL spectra were recorded on a Hitachi F-4500 spectrophotometer at room temperature.

For the *in situ* high pressure measurements, a symmetrical DAC was employed to generate high pressure. A steel gasket was pre-indented to 40 μm thickness followed by laser-drilling the central part to form a 120 μm diameter hole to serve as the sample chamber. Pre-compressed Mn^{4+} -doped BaTiF_6 pellets and ruby ball were loaded in the chamber. In some experiments, neon gas was used as the pressure-transmitting medium (PTM), and the gas loading was performed at GeoSoil-EnviroCARS, Advanced Phonon Source (APS), Argonne National Laboratory (ANL), while in other cases no PTM was used. The pressures were determined by the ruby fluorescence method.⁴⁷ The *in situ* angle-dispersive X-ray diffraction (ADXRD) experiments were carried out at 16 BM-D station of High-Pressure Collaborative Access Team (HPCAT) at APS, ANL. A focused monochromatic X-ray beam with about 5 μm diameter (FWHM) and wavelength of 0.509174 Å was used for the diffraction experiments. The diffraction data were recorded by using a MAR345 image plate and the data were analysed with the Fit2D program.⁴⁸ High-pressure Raman spectroscopic experiments were performed by using a Raman spectrometer with a 532.1 nm excitation laser at High Pressure Synergetic Consortium (HPSynC) at ANL. High-pressure PL spectra were recorded by the same spectrometer with a 30 mW commercial 450 nm laser.

Results and discussion

Syntheses and ambient-pressure characterization of Mn⁴⁺-doped BaTiF₆

Mn⁴⁺-doped BaTiF₆ samples were prepared *via* a one-step hydrothermal method. More than 1 g samples can be obtained within a 50 ml stainless steel autoclave in no more than 1 day, and the Mn doping concentration can be controlled by simply varying the Mn/Ti ratio.³⁰ The as-obtained products are white powders with about 0.4% doping concentration of Mn for Ti in BaTiF₆ by EDS analysis, *e.g.* BaTi_{0.996}Mn_{0.004}F₆. From the TEM images, we can see that the products are sticks with particle sizes ranging from several to several tens of micrometers (Fig. S1†). Fig. 1 presents the Rietveld refinement plot of the ambient powder XRD data of as-obtained Mn-doped BaTiF₆. The pattern can be well fitted by using the trigonal space group *R* $\bar{3}m$ with cell parameters: $a = b = 7.3701(8)$ Å, $c = 7.2526(7)$ Å, which also indicates good purity of the products. Although other elements were also involved in the raw materials, such as potassium in KMnO₄, no K₂TiF₆ or other possible impurity was found. The crystal structure of BaTiF₆ is shown in the insert of Fig. 1. It adopts a trigonal crystal structure comprising of isolated TiF₆ octahedra and their connection with Ba²⁺ ions *via* ionic bonding. Mn⁴⁺ ions are expected to occupy the Ti⁴⁺ positions within the octahedrally coordinated sites. The room temperature PLE and PL spectra at ambient pressure are shown in Fig. 2. Two broad absorption bands centered at about 370 and 468 nm are assigned to the ⁴A_{2g} → ⁴T_{1g} and ⁴A_{2g} → ⁴T_{2g} d-d transitions of octahedrally coordinated Mn⁴⁺ ions, respectively. Under blue light excitation ($\lambda_{\text{ex}} = 468$ nm), the material exhibits red emissions in the 610–660 nm region, and the two strongest peaks centered at 633 and 637 nm can be assigned to the ²E_g → ⁴A_{2g} transition of Mn⁴⁺.

In situ powder XRD and Raman spectroscopy of Mn⁴⁺-doped BaTiF₆

To the best of our knowledge, there is no report on the structural behavior of BaTiF₆ or Mn⁴⁺-doped BaTiF₆ under high

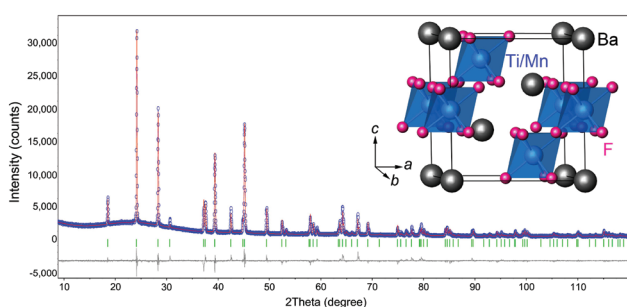


Fig. 1 Rietveld refinement plot of Mn⁴⁺-doped BaTiF₆ at room temperature in the space group *R* $\bar{3}m$, $a = b = 7.3701(8)$ Å, $c = 7.2526(7)$ Å. Experimental data: blue circle; calculated: red line; Bragg reflection positions: green bar; difference: gray line. Insert shows the crystal structure of Mn⁴⁺-doped BaTiF₆ under ambient conditions comprising of isolated (Ti/Mn)F₆ octahedra and Ba²⁺ cations connected with ionic bonding.

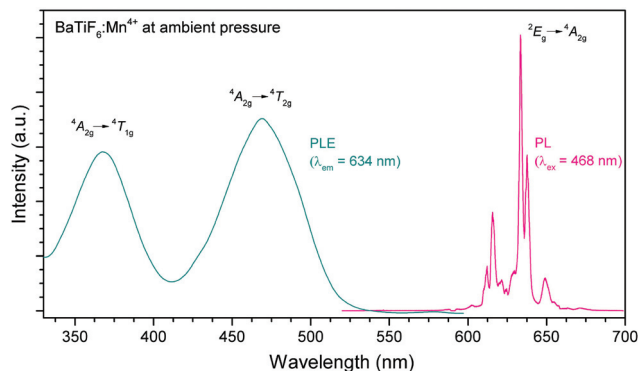


Fig. 2 PLE and PL spectra of Mn⁴⁺-doped BaTiF₆ at room temperature and ambient pressure.

pressure. To check the phase stability of Mn⁴⁺-doped BaTiF₆ under high pressure, *in situ* powder XRD measurements were performed up to 29.8 GPa. In this experiment, neon gas was used as PTM and the XRD patterns of Mn⁴⁺-doped BaTiF₆ as a function of pressure are shown in Fig. 3. At the starting pressure (about 0.5 GPa), the diffraction pattern can be well indexed as a trigonal symmetry, the same as pristine materials. All diffraction peaks shift to higher 2θ values along with the increasing pressure, indicating the decrease of the unit cell and inter atomic distances under compression. Although the diffraction peak intensities change inconsistently, all the peak positions can be well fitted using the trigonal space group *R* $\bar{3}m$ up to 12.9 GPa. Considering no obvious crystal preferred orientation was observed from TEM images, we attribute the inconsistent peak intensity changes to the symmetry lowering to monoclinic (see detailed discussions below along with the Raman data). At 14.4 GPa, there is an obvious broadening or splitting of some peaks (especially the one near $2\theta = 10^\circ$), which indicates further symmetry lowering possibly to tri-

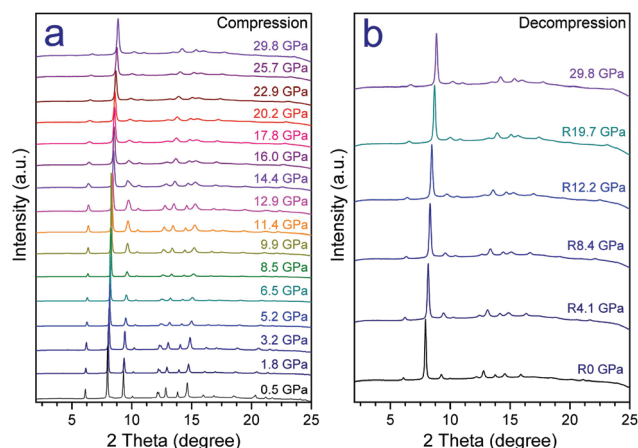


Fig. 3 *In situ* synchrotron powder XRD patterns of Mn⁴⁺-doped BaTiF₆ at room temperature during compression up to 29.8 GPa (a) and decompression (b).

clinic. After that, no additional phase change was observed from the XRD pattern up to 29.8 GPa. Upon decompression, all the diffraction peaks shift to lower 2θ values gradually. The high pressure structure can be maintained at ambient pressure judging from the peak intensity contrast.

Raman spectroscopy was used to gain further insight into the pressure-induced structure evolution of Mn^{4+} -doped BaTiF_6 . Fig. 4 presents the results up to 38.5 GPa at room temperature by using neon gas as PTM. At 0.5 GPa, three peaks at wavenumbers 118, 250 and 617 cm^{-1} are observed and assigned to the vibration of Ba–F bonding, the symmetric bending vibration of $(\text{Ti}/\text{Mn})\text{F}_6$ octahedra (ν_5, T_{2g}), and the symmetric stretching vibration of $(\text{Ti}/\text{Mn})\text{F}_6$ octahedra (ν_1, A_{2g}), respectively (Fig. S2[†]). When subject to higher pressures, the vibration peak from Ba–F bonding disappears gradually, and the ν_1 peak shifts to a higher wavenumber due to the increase of $(\text{Ti}/\text{Mn})\text{–F}$ bonding strength, while the ν_5 stretching vibration splits into two peaks: one shows more blue shift (higher wavenumber) than the other, which indicates possible distortions of the $(\text{Ti}/\text{Mn})\text{F}_6$ octahedron. According to symmetry analyses, there are two possibilities to cause such peak splitting of isolated $(\text{Ti}/\text{Mn})\text{F}_6$ octahedra: one is trigonal distortion along the C_3 -axis (c -direction) which will generate three short $(\text{Ti}/\text{Mn})\text{–F}$ bonds and three longer $(\text{Ti}/\text{Mn})\text{–F}$ bonds, and the trigonal symmetry of the original structure can be maintained; the other possibility is the deviation of $\text{Ti}^{4+}/\text{Mn}^{4+}$ from the center to generate one short and one long apical $(\text{Ti}/\text{Mn})\text{–F}$ bonds, in which situation the crystal symmetry may be lowered to monoclinic. We prefer the latter situation because the displacement of Ti^{4+} in an octahedral site is common to induce ferroelectricity in materials such as BaTiO_3 . So, the conclusion based on the combination of XRD and Raman data is: Mn^{4+} -doped BaTiF_6 adopts a trigonal structure at ambient pressure, then monoclinic between 0.5 and 12.9 GPa, and finally triclinic above 14.4 GPa.

We use the space group $P2_1/m$, the subgroup of $R\bar{3}m$, to perform the LeBail fitting for the 0.5–12.9 GPa XRD pattern,

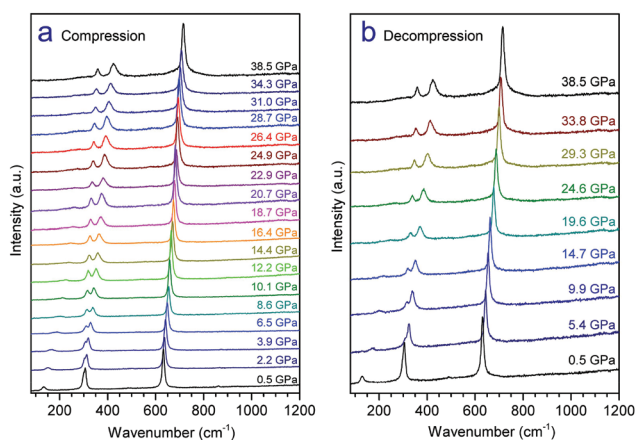


Fig. 4 Raman spectra of Mn^{4+} -doped BaTiF_6 at room temperature during compression up to 38.5 GPa (a) and decompression (b).

and $P\bar{1}$ for the 14.4–29.8 GPa data. Fig. 5 shows the representative powder XRD refinement plots of Mn^{4+} -doped BaTiF_6 at 12.9 GPa and the comparison between monoclinic and triclinic space groups for the pattern taken at 14.4 GPa. It is found that, below 12.9 GPa, all the XRD patterns can be fitted well by using the monoclinic space group $P2_1/m$. Above 14.4 GPa, the triclinic space group $P\bar{1}$ can give better results than the monoclinic one. Note that the space group selection is only based on our powder XRD pattern and the analysis of the Raman evidence. Further experimental characterization is needed to determine the exact space group. The volumes of Mn^{4+} -doped BaTiF_6 were calculated from the refinement results of the XRD patterns, as shown in Fig. 6. The P – V data below 12.9 GPa were used to get the equation of state (EOS) using a third-order Birch–Murnaghan method for the monoclinic phase:⁴⁹

$$P = 3B_0/2[(V/V_0)^{-7/3} - (V/V_0)^{-5/3}]\{1 + 3/4(B_1 - 4) \times [(V/V_0)^{-2/3} - 1]\}$$

where B_0 is the bulk modulus and B_1 is its pressure derivative. The fitting result for the monoclinic phase gives a bulk

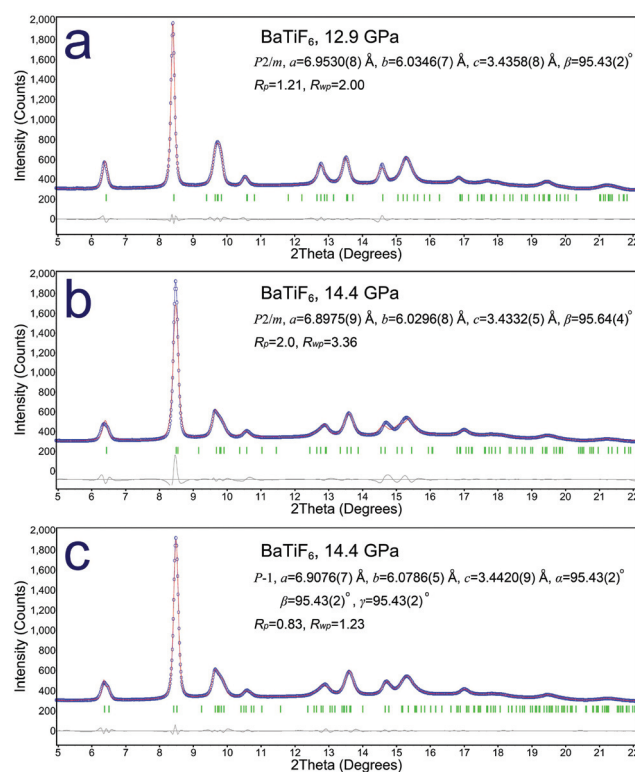


Fig. 5 Rietveld refinement plots of Mn^{4+} -doped BaTiF_6 under different pressures. (a) Refinement of 12.9 GPa XRD with the monoclinic space group $P2_1/m$; (b) refinement of 14.4 GPa XRD data with the space group $P2_1/m$, but significant deviation from experimental data remains; (c) refinement of 14.4 GPa XRD with the triclinic space group $P\bar{1}$ improves both peak positions and R_p and R_{wp} values (experimental data: blue circle; simulation: red line; Bragg reflections: green bar; derives: gray line).

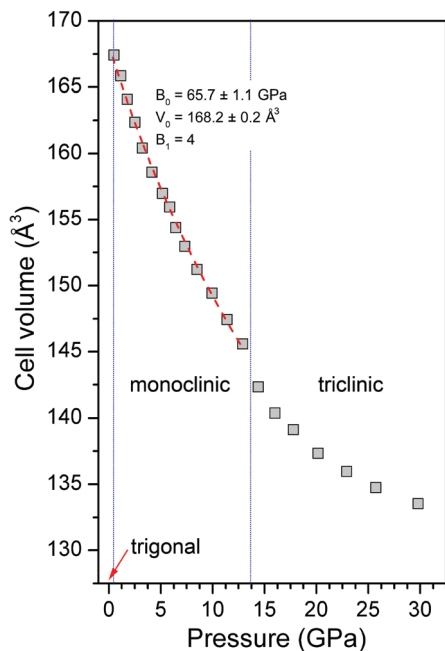


Fig. 6 Unit cell volume evolution of Mn^{4+} -doped BaTiF_6 as a function of pressure at room temperature.

modulus $B_0 = 65.7 \pm 1.1$ GPa at fixed $B_1 = 4.0$. This value indicates that Mn^{4+} -doped BaTiF_6 is a rather soft or compressible material, which is consistent with the loose packing of (Ti/Mn) F_6 octahedra and Ba^{2+} free-ions in the crystal structure (compared to those connected with strong covalent bonding).

Pressure impact on the photoluminescence properties of Mn^{4+} -doped BaTiF_6 red phosphor

Optical properties of transition-metal ion contained materials depend greatly on the local structure around the activator, such as site symmetry and crystal-field strength. The application of high pressure is an efficient way to change the crystal-field strength and also possibly to modify the doping site symmetry. In our experiments, we focused on the two strongest peaks centered at 633 and 637 nm at ambient pressure (denoted as peak 1 and peak 2 hereafter), and discuss their changes as a function of pressure. Fig. 7 shows the position changes of the peaks of Mn^{4+} -doped BaTiF_6 with no PTM.

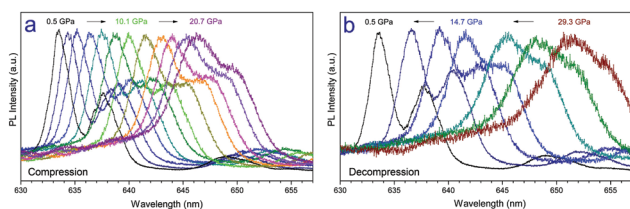


Fig. 7 Red emission spectra of Mn^{4+} -doped BaTiF_6 as a function of pressure with excitation laser at a wavelength of 450 nm at room temperature.

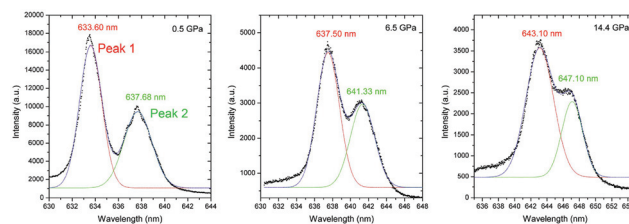


Fig. 8 PL peak fitting results of Mn^{4+} -doped BaTiF_6 at room temperature and representative pressures.

Upon compression, peak 1 shifts gradually to a longer wavelength from 633.6 nm at 0.5 GPa to 646.5 nm at 20.7 GPa. Upon decompression, it goes back to the starting position. Peak fitting analyses were performed to gain more information on the effect of pressure on the PL properties of Mn^{4+} ions in a BaTiF_6 host lattice. Gaussian peak type is used for the splitting of peak 1 and peak 2, and some results are shown in Fig. 8. Although peak 2 does not seem to be a single peak at the lowest pressure (0.5 GPa), no further splitting process is conducted to keep it consistent with the data taken at higher pressures. The PL spectra can be fitted well even when taken at high pressure up to 40 GPa. We also provide the full red emission spectra in a wider range (590–660 nm) of selected pressure points in Fig. S3.†

The peak positions of the red emission of Mn^{4+} -doped BaTiF_6 versus applied pressure are plotted in Fig. 9. The peak 1 and peak 2 lines undergo red shifts, and their positions in wavelength unit (nm) exhibit good linear relationship with pressure. No abnormal change is observed despite the symmetry lowering during the two pressure-induced phase transitions. This phenomenon indicates that the two above-mentioned structural changes may relate to the slow rotation

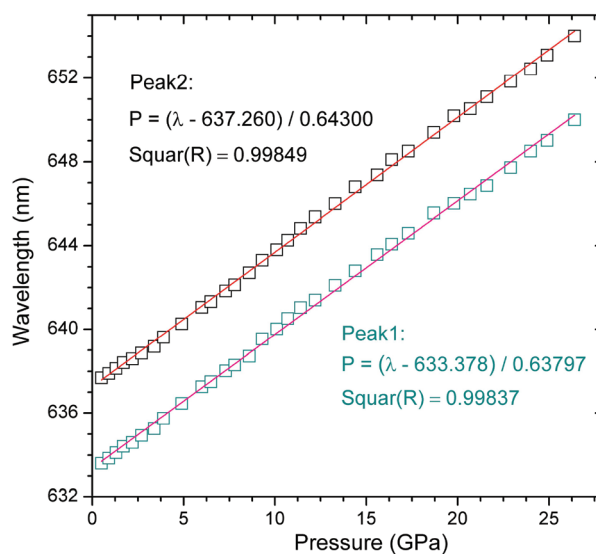


Fig. 9 Linear fitting of the peak positions of Mn^{4+} -doped BaTiF_6 at room temperature and different pressures.

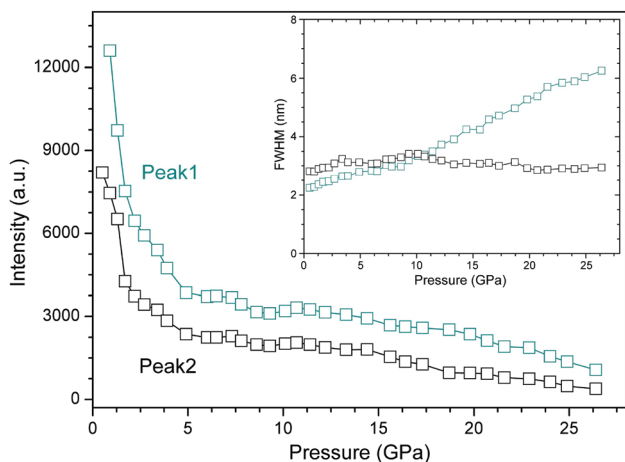


Fig. 10 PL intensity of Mn^{4+} -doped BaTiF_6 at room temperature as a function of applied pressure. Insert shows the evolution of full-width-at-half-maximum (FWHM) of the two peaks as a function of pressure.

or realignment of isolated $(\text{Ti}/\text{Mn})\text{F}_6$ units, but no sudden changes (such as bond-breaking) within the octahedra. The pressure coefficients of peak 1 and peak 2 lines of Mn^{4+} are equal to $0.63797 \text{ nm GPa}^{-1}$ and $0.64300 \text{ nm GPa}^{-1}$, respectively. We also represent the evolution of peak intensities and Full-Width-at-Half-Maximum (FWHM) of peak 1 and peak 2 as a function of pressure in Fig. 10. The emission intensity drops quickly in the low pressure region ($<5 \text{ GPa}$), which can be attributed to the quick reduction of the sample thickness. After that, it remains smooth and steady up to nearly 30 GPa . The broadening of the two peaks is moderate and acceptable as a pressure probe judging from the change of FWHM along with the increasing pressure. All these results demonstrate hydrostatic pressure as a useful tool for modifying the emitting properties of phosphors, for example to make warm WLED warmer. On the other hand, transition metal ion activated materials such as Mn^{4+} -doped BaTiF_6 may find potential applications as pressure gauges for high pressure techniques.

Finally, we performed a detailed comparison of the pressure-involved PL behavior between Mn^{4+} -doped BaTiF_6 and ruby (Cr^{3+} -doped Al_2O_3 , a currently used pressure gauge).^{46,47} Neon gas was used as the PTM to generate quasi-hydrostatic pressure in this experiment and the two emission peaks of ruby are denoted as peak 1 and peak 2 (Fig. S4†). Fig. 11a shows the relationship between the emission peak positions and applied pressure of Mn^{4+} -doped BaTiF_6 and ruby. All of the four emission peaks undergo red shifts, and their positions in wavelength unit (nm) show a good linear relationship with the pressure up to 40 GPa . The Mn^{4+} -doped BaTiF_6 shows larger pressure coefficients ($0.66553 \text{ nm GPa}^{-1}$ for peak 1, $0.69196 \text{ nm GPa}^{-1}$ for peak 2) than those of ruby ($0.34032 \text{ nm GPa}^{-1}$ for peak 1, $0.35174 \text{ nm GPa}^{-1}$ for peak 2). This can be attributed to the better compressibility of Mn^{4+} -doped BaTiF_6 than that of ruby. And thus, a better resolution is expected when Mn^{4+} -doped BaTiF_6 is used as a pressure

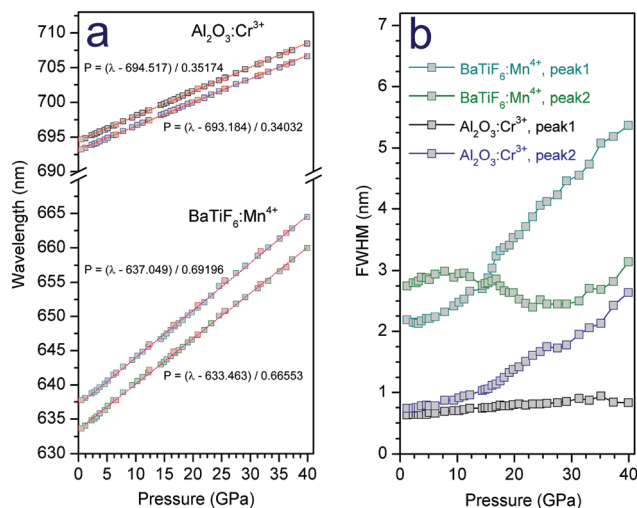


Fig. 11 Linear fitting of the peak positions (a) and FWHM (b) of Mn^{4+} -doped BaTiF_6 and ruby (Cr^{3+} -doped Al_2O_3) at room temperature and hydrostatic pressure. Ne gas is used as the pressure intermediate. Red squares in (a) are measurements during pressure decompression which are not used in the linear fitting.

sensor. In addition, larger pressure coefficients are observed for Mn^{4+} -doped BaTiF_6 in a better hydrostatic pressure environment than those measured without PTM.

The comparisons of FWHM and emission intensity between Mn^{4+} -doped BaTiF_6 and ruby are shown in Fig. 11b and 12. Mn^{4+} -doped BaTiF_6 exhibits broader emission peaks than those of ruby. Nevertheless, the peak widths and the broadening at higher pressure up to 40 GPa are still acceptable to do a pattern fitting. Upon compression, all the four emis-

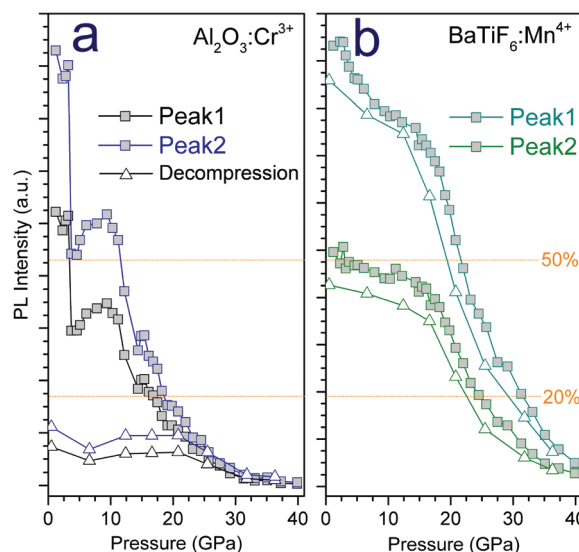


Fig. 12 PL intensity of ruby (Cr^{3+} -doped Al_2O_3) (a) and Mn^{4+} -doped BaTiF_6 (b) at room temperature and different pressures. Ne gas is used as the pressure intermediate.

sion peaks become weaker along with the increasing pressure. Mn⁴⁺-doped BaTiF₆ shows a slower emission quenching under applied high pressure than that of ruby (50% intensity remains above 20 GPa, 20% above 30 GPa). Considering these advantages together with the facile synthesis route, Mn⁴⁺-doped BaTiF₆ or other transition metal activated fluorides may find specific applications in the high pressure techniques.

Conclusions

In summary, we have investigated the effect of pressure on the structure and PL properties of a Mn⁴⁺ ion within BaTiF₆ host material by means of *in situ* synchrotron X-ray diffraction, Raman and PL spectroscopy techniques. The material shows strong and stable red emission bands up to about 40 GPa. The linear shift of the red emission peaks of octahedrally coordinated Mn⁴⁺ as a function of applied pressure provides a new technique and understanding into the crystal-field tuning of optical properties. Detailed comparisons of the pressure effect on PL properties between Mn⁴⁺-doped BaTiF₆ and ruby (Cr³⁺-doped Al₂O₃, a currently used pressure gauge) were performed using neon gas as the pressure transmission medium. Due to their stable emission behavior under high pressure, low-cost and facile synthesis route, Mn⁴⁺-doped BaTiF₆ together with other Mn⁴⁺-doped fluorides shed light on the exploitation of Mn⁴⁺ spectroscopy within specific host lattices as an alternative pressure probe for the DAC technique.

Acknowledgements

The UNLV High Pressure Science and Engineering Center (HIPSEC) is a DOE–NNSA Center of Excellence supported by Cooperative Agreement DE-NA0001982. This research was supported by DOE-BES X-ray Scattering Core Program under grant number DE-FG02-99ER45775. HPCAT operations were supported by DOE-NNSA under award no. DE-NA0001974 and DOE-BES under award no. DE-FG02-99ER45775, with partial instrumentation funding by NSF. The gas loading was performed at GeoSoilEnviroCARS, APS, ANL, supported by EAR-1128799 and DE-FG02-94ER14466. APS is supported by DOE-BES, under contract no. DE-AC02-06CH11357. The authors thank Q. Li, R. Ferry, and S. Tkachev for their valuable suggestions and technical support.

Notes and references

- S. Nakamura, T. Mukai and M. Senoh, *Appl. Phys. Lett.*, 1994, **64**, 1687.
- C. C. Yang, H. Y. Tsai and K. C. Huang, *Opt. Rev.*, 2013, **20**, 232.
- M. Huang and L. Yang, *IEEE Photonics Technol. Lett.*, 2013, **25**, 1317.
- E. F. Schubert and J. K. Kim, *Science*, 2005, **308**, 1274.
- L. Chen, Y. Zhang, F. Y. Liu, A. Q. Luo, Z. X. Chen, Y. Jiang, S. F. Chen and R.-S. Liu, *Mater. Res. Bull.*, 2012, **47**, 4071.
- R.-J. Xie and N. Hirosaki, *Sci. Technol. Adv. Mater.*, 2007, **8**, 588.
- K. Sakuma, K. Omichi, N. Kimura, M. Ohashi, D. Tanaka, N. Hirosaki, Y. Yamamoto, R.-J. Xie and T. Suehiro, *Opt. Lett.*, 2004, **29**, 2001.
- Y. Sato, H. Kato, M. Kobayashi, T. Masaki, D.-H. Yoon and M. Kakihana, *Angew. Chem., Int. Ed.*, 2014, **53**, 7756.
- S. Schmiechen, H. Schneider, P. Wagatha, C. Hecht, P. J. Schmidt and W. Schnick, *Chem. Mater.*, 2014, **26**, 2712.
- P. Pust, V. Weiler, C. Hecht, A. Tücks, A. S. Wochnik, A.-K. Henß, D. Wiechert, C. Scheu, P. J. Schmidt and W. Schnick, *Nat. Mater.*, 2014, **13**, 891.
- T.-C. Liu, B.-M. Cheng, S.-F. Hu and R.-S. Liu, *Chem. Mater.*, 2011, **23**, 3698.
- X.-M. Wang, C.-H. Wang, X.-J. Kuang, R.-Q. Zou, Y.-X. Wang and X.-P. Jing, *Inorg. Chem.*, 2012, **51**, 3540.
- W. B. Park, S. P. Singh, C. Yoon and K.-S. Sohn, *J. Mater. Chem. C*, 2013, **1**, 1832.
- H. Nersisyan, H. I. Won and C. W. Won, *Chem. Commun.*, 2011, **47**, 11897.
- J. Li, T. Watanabe, N. Sakamoto, H. Wada, T. Setoyama and M. Yoshimura, *Chem. Mater.*, 2008, **20**, 2095.
- Y. Hu, W. Zhuang, H. Ye, S. Zhang, Y. Fang and X. Huang, *J. Lumin.*, 2005, **111**, 139.
- R. Jabbarov, N. Musayeva, F. Scholz, T. Wunderer, A. N. Turkin, S. S. Shirokov and A. E. Yunovich, *Phys. Status Solidi A*, 2009, **206**, 287.
- J. Thirumalai, R. Chandramohan, S. Auluck, T. Mahalingam and S. R. Srikumar, *J. Colloid Interface Sci.*, 2009, **336**, 889.
- M. H. Du, *J. Mater. Chem. C*, 2014, **2**, 2475.
- L. Chen, S. Xue, X. Chen, A. Bahader, X. Deng, E. Zhao, Y. Jiang, S. Chen, T.-S. Chan, Z. Zhao and W. Zhang, *Mater. Res. Bull.*, 2014, **60**, 604.
- A. M. Srivastava and M. G. Brik, *J. Lumin.*, 2012, **132**, 579.
- W. Lü, W. Lv, Q. Zhao, M. Jiao, B. Shao and H. You, *Inorg. Chem.*, 2014, **53**, 11985.
- R. Kasa and S. Adachi, *J. Electrochem. Soc.*, 2012, **159**, J89.
- T. Takahashi and S. Adachi, *J. Electrochem. Soc.*, 2008, **155**, E183.
- Y. K. Xu and S. Adachi, *J. Appl. Phys.*, 2009, **105**, 013525.
- T. Arai and S. Adachi, *J. Appl. Phys.*, 2011, **110**, 063514.
- H.-L. Jeong and Y.-D. Huh, *Mater. Lett.*, 2010, **64**, 1816–1818.
- J. Liu, N. Du, P. Wu, J. Wang, H. Zhang and D. Yang, *Mater. Res. Bull.*, 2012, **47**, 3923–3926.
- H.-D. Nguyen, C. C. Lin, M.-H. Fang and R.-S. Liu, *J. Mater. Chem. C*, 2014, **2**, 10268.
- X. Jiang, Y. Pan, S. Huang, X. Chen, J. Wang and G. Liu, *J. Mater. Chem. C*, 2014, **2**, 2301.
- X. Jiang, Z. Chen, S. Huang, J. Wang and Y. Pan, *Dalton Trans.*, 2014, **43**, 9414.
- L. Lv, X. Jiang, S. Huang, X. Chen and Y. Pan, *J. Mater. Chem. C*, 2014, **2**, 3879–3884.
- L.-L. Wei, C. C. Lin, M.-H. Fang, M. G. Brik, S.-F. Hu, H. Jiao and R.-S. Liu, *J. Mater. Chem. C*, 2015, **3**, 1655–1660.

- 34 H. Zhu, C. C. Lin, W. Luo, S. Shu, Z. Liu, Y. Liu, J. Kong, E. Ma, Y. Cao, R.-S. Liu and X. Chen, *Nat. Commun.*, 2014, **5**, 4312.
- 35 G. Li, C. C. Lin, W.-T. Chen, M. S. Molocheev, V. V. Atuchin, C.-Y. Chiang, W. Zhou, C.-W. Wang, W.-H. Li, H.-S. Sheu, T. S. Chan, C. Ma and R.-S. Liu, *Chem. Mater.*, 2014, **26**, 2991.
- 36 W.-T. Chen, H.-S. Sheu, R.-S. Liu and J. P. Attfield, *J. Am. Chem. Soc.*, 2012, **134**, 8022.
- 37 S.-S. Wang, W.-T. Chen, Y. Li, J. Wang, H.-S. Sheu and R.-S. Liu, *J. Am. Chem. Soc.*, 2013, **135**, 12504.
- 38 W.-Y. Huang, F. Yoshimura, K. Ueda, Y. Shimomura, H.-S. Sheu, T.-S. Chan, H. F. Greer, W. Zhou, S.-F. Hu, R.-S. Liu and J. P. Attfield, *Angew. Chem., Int. Ed.*, 2013, **52**, 8102.
- 39 Q. Li, S. Li, K. Wang, J. Liu, B. Liu, K. Yang and B. Zou, *J. Phys. Chem. C*, 2014, **118**, 7562.
- 40 Y. Ma, M. Eremets, A. R. Oganov, Y. Xie, I. Trojan, S. Medvedev, A. O. Lyakhov, M. Valle and V. Prakapenka, *Nature*, 2009, **458**, 182.
- 41 J. Barzowska, K. Szczodrowski, M. Krosnicki, B. Kuklinski and M. Grinberg, *Opt. Mater.*, 2012, **34**, 2095.
- 42 M. Grinberg, J. Barzowska, A. Baran and B. Kuklinski, *Mater. Sci. -Pol.*, 2011, **29**, 272.
- 43 S. Mahlik, A. Lazarowska, M. Grinberg, T.-C. Liu and R.-S. Liu, *J. Phys. Chem. C*, 2013, **117**, 13181.
- 44 L. Wang, Y. Pan, Y. Ding, W. Yang, W. L. Mao, S. V. Sinogeikin, Y. Meng, G. Shen and H. K. Mao, *Appl. Phys. Lett.*, 2009, **94**, 061921.
- 45 H. Yuan, K. Wang, S. Li, X. Tan, Q. Li, T. Yan, B. Cheng, K. Yang, B. Liu, G. Zou and B. Zou, *J. Phys. Chem. C*, 2012, **116**, 24837.
- 46 H. K. Mao, P. M. Bell, J. W. Shaner and D. J. Steinberg, *J. Appl. Phys.*, 1987, **49**, 3276.
- 47 H. K. Mao, J. Xu and P. M. Bell, *J. Geophys. Res.*, 1986, **91**, 4673.
- 48 A. P. Hammersley, S. O. Svensson and M. Hanfland, *High Pressure Res.*, 1996, **14**, 235.
- 49 F. Birch, *Phys. Rev.*, 1947, **71**, 809.